Reconstruction of multi-phase parametric maps in four-dimensional magnetic resonance fingerprinting (4D-MRF) by optimization of local T1 and T2 sensitivities

Yat Lam Wong

Department of Health Technology and Informatics, The Hong Kong Polytechnic University, Hong Kong;

Department of Clinical Oncology, Queen Mary Hospital, Hong Kong

Tian Li

Department of Health Technology and Informatics, The Hong Kong Polytechnic University, Hong Kong

Chenyang Liu

Department of Health Technology and Informatics, The Hong Kong Polytechnic University, Hong Kong

Ho-Fun Victor Lee

Department of Clinical Oncology, The University of Hong Kong, Hong Kong

Lai-Yin Andy Cheung

Department of Clinical Oncology, The University of Hong Kong, Hong Kong

Edward Sai Kam Hui

Department of Rehabilitation Science, The Hong Kong Polytechnic University, Hong Kong

Peng Cao

Department of Diagnostic Radiology, The University of Hong Kong, Hong Kong

Jing Cai

Department of Health Technology and Informatics, The Hong Kong Polytechnic University, Hong Kong

Corresponding Author

Jing Cai, Ph.D.

Department of Health Technology and Informatics

The Hong Kong Polytechnic University

11 Yuk Choi Rd, Hung Hom

Hong Kong, China

Tel: (852) 3400 8645

Email: jing.cai@polyu.edu.hk

Peng Cao, Ph.D.

Department of Diagnostic Radiology

The University of Hong Kong

5 Sassoon Road, Pokfulam

Hong Kong

Short title: Reconstruction of 4D-MRF by optimization of T1 and T2 sensitivities

Background: Time-resolved magnetic resonance fingerprinting (MRF), or 4D-MRF, has been demonstrated its feasibility in motion management in radiotherapy (RT). However, the prohibitive long acquisition time is one of challenges of the clinical implementation of 4D-MRF. The shortening of acquisition time causes data insufficiency in each respiratory phase, leading to poor accuracies and consistencies of the predicted tissues' properties of each phase.

Purpose: To develop a technique for the reconstruction of multi-phase parametric maps in four-dimensional magnetic resonance fingerprinting (4D-MRF) through the optimization of local T1 and T2 sensitivities.

Methods: The proposed technique employed an iterative optimization to tailor the data arrangement of each phase by manipulation of inter-phase frames, such that the T1 and T2 sensitivities, which were quantified by the modified Minkowski distance, of the truncated signal evolution curve was maximized. The multi-phase signal evolution curves were modified by sliding window reconstruction and inter-phase frame sharing (SWIFS). Motion correction and dot product matching were sequentially performed on the modified signal evolution and dictionary to reconstruct the multi-parametric maps. The proposed technique was evaluated by numerical simulations using the extended cardiac-torso (XCAT) phantom with regular and irregular breathing patterns, and by in vivo MRF data of 3 health volunteers and 6 liver cancer patients acquired at a 3.0 T scanner.

Results: In simulation study, the proposed SWIFS approach achieved the overall mean absolute percentage error (MAPE) of 8.62% ± 1.59% and 16.2% ± 3.88% for the eight-phases T1 and T2 maps, respectively, in the sagittal view with irregular breathing pattern. In contrast, the overall MAPE of T1 and T2 maps generated by the conventional approach with multiple MRF repetitions were 22.1% ± 11.0% and 30.8% ± 14.9%, respectively. For in-vivo study, the predicted mean T1 and T2 of liver by the proposed SWIFS approach were 795ms ± 38.9ms and 58.3ms ± 11.7ms, respectively.

Conclusions:

Both simulation and in vivo results showed that the approach empowered by T1 and T2 sensitivities optimization and sliding window under the shortened acquisition of MRF had superior performance in the estimation of multi-phase T1 and T2 maps as compared to conventional approach with oversampling of MRF data.

Keywords: MR Fingerprinting, 4D Imaging, Abdominal MRI, Liver Cancer, Motion Management

1. INTRODUCTION

Tumor motion induced by respiration leads to a sub-optimal delivery of radiation in radiotherapy. Four-dimensional (4D) imaging, or respiration-correlated imaging, which incorporates tumor movement and 3D-anatomical information, enabled by computed tomography (CT) is routinely used in radiotherapy for tumor motion management. [1] However, limitations of 4D-CT, including poor soft tissue contrast, motion artifacts, need for administration of contrast agent, and radiation dose, urge for the search of alternatives to 4D-CT for radiotherapy. [2,3] 4D-MRI is an emerging dynamic imaging technique to provide better soft tissue distinguishability as compared to 4D-CT and it has been studied intensively. [4-8]

Recently, magnetic resonance fingerprinting (MRF) has been proposed to be a powerful quantitative imaging technique that can permit the estimation of multiple magnetic resonance parameters in a single scan based on a pseudorandom acquisition. [9-11] This can eliminate the errors resulting from the registration of images with different contrasts acquired by separated MRI sequences. [12] Besides providing anatomical information, quantitative tissue properties derived from MRF could help to characterize tumor heterogeneity. [9,13,14] For instance, retrospective synthesis of MR images with mixed T1 and T2 contrast can be achieved. Due to the high temporal resolution rendered by the highly undersampled dynamic MRF acquisition, dynamic imaging based on MRF, namely time-resolved MRF or 4D-MRF, has demonstrated its feasibility in motion management in radiotherapy. [12,15] Till now, one of the challenges of the clinical implementation of MRF is the prohibitive long acquisition time for multi-phase and multi-slice coverage. [9,15,16] The shortening of acquisition time may result in compromising the parametric maps' accuracy due to undersampling artifacts. [9] Nevertheless, these can be mitigated by the implementation of advanced iterative reconstruction algorithm realized by compressed sensing (CS) and alternative direction method of multipliers (ADMM) with low-rank (LR) approximation on dictionary and voxels' signal evolution. [17-20] These iterative reconstruction techniques generally involve a simultaneous enforcement of consistency between k-space data and image domain, and penalty functions, to suppress aliasing artifacts in the image domain. Another non-iterative technique that involves sliding window reconstruction of consecutive MRF dynamic images for enhancing the MRF dictionary matching accuracy has been proposed by Cao et al. [21] The authors demonstrated a time-efficient and robust dictionary matching in the sliding window domain by the suppression of incoherent aliasing artifacts and noises with the sliding window reconstruction, hence achieving a decrease in number of temporal points required in dictionary matching.

In 4D-MRF, where retrospective phase binning of MRF data for defining the physiological motion states is necessary, prolonged MRF scanning time is required to ensure an adequate number of frames in each phase bin. [15,16] Moreover, originally continuous signal evolution is irregularly truncated after the phase sorting process, leading to incomplete signal evolution curves in some phases. Under these

circumstances, the T1 and T2 sensitivities of the MRF data in each phase bin can be highly inconsistent due to the irregular breathing of patients. Efforts have been made to address this issue from two aspects. In the pulse sequence design aspect, inversion recovery (IR) and T2 preparation pulses are employed in the acquisition to increase the T1 and T2 sensitivities. [22] In the image reconstruction aspect, motion differences of each phase are compensated by nonrigid image registration, whereby images of other phases are registered to the target phase before dictionary matching to recover the complete signal evolution for each phase. [23,24] However, for single slice or cine MRF acquisition, the nonrigid image registration can only be performed in a slice-by-slice manner due to the inter-slice intensity variation. The incomplete correction of the through-plane motion may result in reduction of parametric maps' accuracies. [23]

In this work, we demonstrated some metrics for the quantification of the local T1 and T2 sensitivities of 4D-MRF data. Based on these metrics, we also proposed a reconstruction technique, Sliding Window Inter-phase Frame Sharing (SWIFS), which utilized an iterative algorithm for maximizing the T1 and T2 sensitivities for each phase by manipulating inter-phase data. This technique aims to address the issue of data insufficiency in phase bins due to the retrospective phase sorting process by allocating small amounts, but impactful, data to the target phase, without significant disturbance of inter-bin motion information. The proposed technique was tested using 4D-extended Cardiac-Torso (XCAT) phantom simulations, healthy volunteer data, and liver cancer patient data.

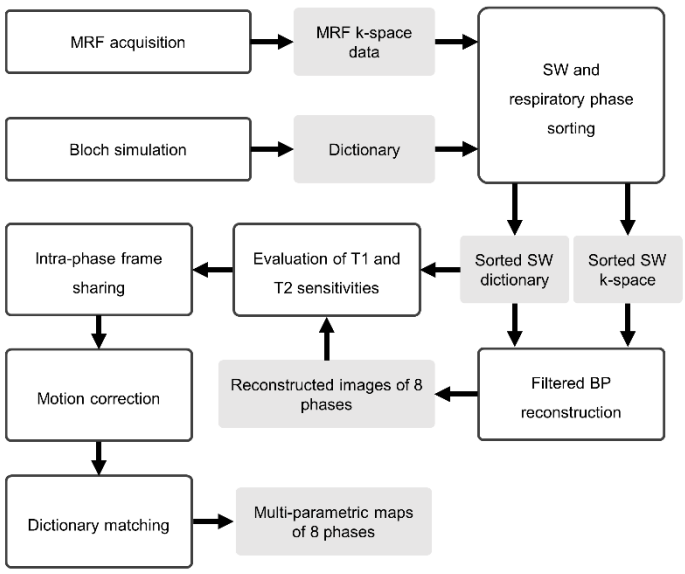

Figure 1 Workflow of the proposed 4D-MRF framework, consisting of six steps: (1) MRF acquisition, (2) dictionary simulation, (3) sliding window (SW) combination of k-space data and phase sorting, (4) filtered back-projection (BP) reconstruction, (5) inter-phase frame sharing and motion correction, and (6) dictionary matching.

2. METHODS AND MATERIALS

The proposed 4D-MRF framework is summarized in the schematic diagram in **Figure 1**. It is composed of six steps: (1) MRF acquisition, (2) dictionary simulation, (3) sliding window (SW) combination of k-space data and phase sorting, (4) filtered back-projection (BP) reconstruction, (5) SWIFS and motion correction, and (6) dictionary matching. The implementation of these steps will be described in this section in detail.

2.A In vivo MRF acquisition

Three healthy volunteers and six liver cancer patients were recruited in the study under an Institutional Review Board-approved protocol. The MRF scans were performed on a 3.0 T MRI scanner (GE Healthcare) with a 50-channel "AIR" coil for signal reception. An inversion recovery FISP sequence with the following scanning parameters was adopted in the experiments (Figure S1). A spiral out readout trajectory was used in each TR and a rotation of 222.5^{o} was applied from one TR to the next TR, with a total of 377 spiral interleaves in 1000 dynamics. The flip angle varied from 0 ^{o} to 70 ^{o} and followed a "half-sinc"-style. The TR in each MRF repetition varied from 11.7 to 14.3 ms, and TE = 1.77 ms was fixed throughout the acquisition. A single sagittal slice was scanned with a total number of 10 MRF repetitions for each volunteer and 2 MRF repetitions for each patient. The scanning time was 13 s for 1 MRF repetition. The MRF repetitions were started at the end of exhalation and scanned under free breathing condition. The slice thickness, field of view, and matrix size were 5 mm, 300 × 300 mm^2, and 256 × 256, respectively.

2.B Dictionary simulation

The MRF dictionary simulations of the signal evolution in the inversion recovery unbalanced steady state free precession acquisition were implemented using the extended phases graph (EPG) algorithm. [25] Field inhomogeneity, slice profile, diffusion, and magnetization transfer effects were not considered in this work. Signal evolutions with the following T1 and T2 were simulated: T1 = [2:2:100, 120:20:2000, 2040:40:3000] ms; T2 = [2:2:130, 140:10:200, 220:20:1000, 1040:40:2000] ms.

2.C Sliding window technique

Sliding window strategy was applied to the acquired MRF k-space raw data based on the methods proposed by Cao et al. with some modifications. [21] Essentially, the k-space of a sliding window frame can be constructed by the superposition of the k-space of numerous consecutive spiral interleaves. The

k-space of each channel for the j th sliding window frame ($\mathbf{S}_j$) with the window size w and stride d can be expressed as:

$$\mathbf{S}_j = [\mathbf{S}_{i=d\cdot(j-1)+1}, \mathbf{S}_{i=d\cdot(j-1)+2}, \cdots, \mathbf{S}_{i=d\cdot(j-1)+w}] \quad [1]$$

, where $\mathbf{S}_i$ is the k-space data acquired from the scanner. By so doing, the total number of frames in a single MRF repetition will be decreased from 1000 in the original domain to $(1000 - w)/d + 1$ in the sliding window reconstruction framework.

The sliding window image can be obtained by the filtered BP: [17,21]

$$\mathbf{X}_j = \mathbf{F}_j^H \cdot \mathbf{G}_{dc}^H \cdot \mathbf{S}_j \quad [2]$$

, where $\mathbf{G}_{dc}^H$ is the density compensation and regridding operator, $\mathbf{F}_j^H$ is the nonuniform fast Fourier transform (NUFFT) operator, and the superscript ^{H} denotes the Hermitian conjugate. The dictionary is modified accordingly to accommodate to the sliding window signal evolution:

$$\mathbf{D}_j = \sum_{i=d\cdot(j-1)+1}^{d\cdot(j-1)+w} \mathbf{D}_i \quad [3]$$

, where i and j represent the index of image in the original domain and sliding window domain, respectively. Hereafter, the sliding window parameters of w = 30 and d = 10 were used in this work, and "sliding window frame" will simply be denoted as "frame" unless stated otherwise.

2.D Respiratory phase sorting

Before the respiratory phase sorting of MRF data, the surrogate signal of volunteer or patient was extracted retrospectively based on the diaphragm motion using an in-house MATLAB (The MathWorks, Inc.) tool. In brief, a pencil-shape region-of-interest (ROI) with the size 30 pixels x 2 pixels was placed across the diaphragm at the first sliding window frame. The ROI was duplicated to the same position at other frames to construct a diaphragm profile with the time-series of images. The diaphragm profile underwent normalization and Hanning filtering to remove the variation in contrast and noises, respectively. Active contouring was implemented on the diaphragm profile to extract the diaphragm motion curve. The final surrogate signal was an average of five diaphragm motion curves obtained by the abovementioned process with the ROIs adjacent to the pre-selected ROIs.

After the extraction of surrogate signal, the sliding window k-space and the sliding window dictionary as formulated by [1] and [3] were retrospectively sorted into eight respiratory phases based on the surrogated signal. To retain the hysteresis and the probabilistic information of respiration for radiotherapy planning, the temporal phase sorting approach with fixed bin-width was utilized in this work. [5] The phase sorting method for MRF data used here was adopted from our previous work, except

the phase sorting was performed in the sliding window domain instead of the original domain. Further details of the phase sorting method for 4D-MRF can be found in these references. [15,16]

2.F Quantification of T1 and T2 sensitivities

Distinguishability between two signal evolution curves can be quantified by the second-order Minkowski distance (MD) [21] :

$$\mathrm{MD}_{\boldsymbol{x,y}} = \left(\sum_{i=1}^{T_p} \left|\mathbf{D}_{x,i} - \mathbf{D}_{y,i}\right|^2\right)^{1/2} \quad [4]$$

, where $\mathbf{D}_x$ and $\mathbf{D}_y$ are two different dictionary elements; T_p is the total number of frames in phase p . By plugging in the dictionary elements with different T1 and fixed T2 (or different T2 and fixed T1), the resulting MD magnitude indicates the dictionary sensitivity to T1 (or T2). In this work, the concept of MD is further extended to consider the local dictionary sensitivity as a function of T1 and T2:

$$\mathbf{MD}_{T1}(T1,T2) = \left[\sum_{i=1}^{T_p} |\mathbf{D}_i(T1 + \Delta\mathrm{t}_1, T2) - \mathbf{D}_i(T1 - \Delta\mathrm{t}_1, T2)|^2\right]^{1/2} \quad [5]$$

$$\mathbf{MD}_{T2}(T1,T2) = \left[\sum_{i=1}^{T_p} |\mathbf{D}_i(T1, T2 + \Delta\mathrm{t}_2) - \mathbf{D}_i(T1, T2 - \Delta\mathrm{t}_2)|^2\right]^{1/2} \quad [6]$$

$\Delta\mathrm{t}_1$= 0.05s and $\Delta\mathrm{t}_2$ = 0.005 s was used in all experiments. Now, $\mathbf{MD}_{T1}$ and $\mathbf{MD}_{T2}$ can be directly interpreted as the dictionary sensitivity to T1 and T2, respectively, for specific tissue with the defined T1 and T2 relaxation times.

Derivatives of magnetization (DOM) was also utilized in this work to depict the dictionary sensitivity in another perspective. [26] DOM with respective to T1 (or T2) is defined as the change in transverse magnetization with respect to the change in tissue's T1 (or T2) relaxation time. In the context of MRF, the dictionary, which is calculated using EPG formulism to model the resulting signal reception, can directly represent the transverse magnetization. Assume the central differencing approximation is valid under small $\Delta\mathrm{t}_1$ and $\Delta\mathrm{t}_2$, the DOM with respect to T1 and T2 are given by:

$$\frac{\mathrm{d}\mathbf{D}}{\mathrm{dT1}} \cong \frac{\mathbf{D}(\mathrm{T1}+\Delta\mathrm{t}_1,\mathrm{T2}) - \mathbf{D}(\mathrm{T1}-\Delta\mathrm{t}_1,\mathrm{T2})}{2\Delta\mathrm{t}_1} \quad [7]$$

$$\frac{\mathrm{d}\mathbf{D}}{\mathrm{dT2}} \cong \frac{\mathbf{D}(\mathrm{T1},\mathrm{T2}+\Delta\mathrm{t}_2) - \mathbf{D}(\mathrm{T1},\mathrm{T2}-\Delta\mathrm{t}_2)}{2\Delta\mathrm{t}_2} \quad [8]$$

In this work, $\Delta\mathrm{t}_1$= 0.05s and $\Delta\mathrm{t}_2$ = 0.005 s were used. In [7] and [8], DOM is a function of tissue properties (T1 and T2 relaxation times) and frame index. This renders the power to DOM to describe the dictionary sensitivity for certain frame index.

2.G Sliding Window Inter-phase Frame Sharing (SWIFS) and motion correction (MC)

Inter-phase frame sharing duplicates the image frames from phase p' and allocate it to the target phase p, such that the new signal evolution curve of phase p manifests an enhancement of T1 and T2 sensitivities in dictionary matching, and hence, increases accuracy of the resulting parametric maps. Assume the image series of phase p, $\mathbf{X}_p$, has a total number of T_p image frames, an image $\mathbf{X}_{p',t_{p'}}$ in phase p' is allocated to the target phase p and becomes $\mathbf{X}_{p,T_p+1}$. Multiple frames from other phases can be added into the target phase p in the same manner, and they are denoted accordingly as $[\mathbf{X}_{p,T_p+1}, \mathbf{X}_{p,T_p+2}, \cdots]$. The total number of image frames in phase p then becomes T_p'.

The modified image series of the target phase p after the frame sharing, $\mathbf{X}_p'$, is given by:

$$\mathbf{X}_p' = \left[\mathbf{X}_{p,1}, \mathbf{X}_{p,2}, \cdots, \mathbf{X}_{p,t_p}, \cdots, \mathbf{X}_{p,T_p}, \mathbf{X}_{p,T_p+1}, \mathbf{X}_{p,T_p+2}, \cdots\right] \quad [9]$$

To compensate the inter-phase motion variation, deformable vector field (DVF), $\boldsymbol{R}_{p'\to p}$, is applied to correct the reparatory motion of the shared frame prior to the frame allocation:

$$\mathbf{X}_{p,T_p+1} = \boldsymbol{R}_{p'\to p} \cdot \mathbf{X}_{p',t_{p'}} \quad [10]$$

Similar manipulation is performed accordingly to the dictionary:

$$\mathbf{D}_p' = \left[\mathbf{D}_{p,1}, \mathbf{D}_{p,2}, \cdots, \mathbf{D}_{p,t_p}, \cdots, \mathbf{D}_{p,T_p}, \mathbf{D}_{p,T_p+1}, \mathbf{D}_{p,T_p+2}, \cdots\right] \quad [11]$$

To optimize the inter-phase shared frames, $\mathbf{X}_{p',t_{p'}}$, that benefit the accuracy and precision of parametric maps at the target phase p, we can simply set up a minimization problem that aims to maximize the dictionary sensitivity of $\mathbf{D}_p'$ as represented by the abovementioned quantities:

$$\arg\min_{\mathbf{D}_p'} \sum_{T1,T2} \left[-\mathbf{W}_1 \cdot \mathbf{MD}_{\mathrm{T1}}^{\mathbf{D}_p'}(T1,T2) - \mathbf{W}_2 \cdot \mathbf{MD}_{\mathrm{T2}}^{\mathbf{D}_p'}(T1,T2)\right] + W_3 \cdot \sum_{t_p=T_p+1}^{T_p+n_p} \left|A_{t_p} - A_p\right| \quad [12]$$

$\mathbf{W}_1$ and $\mathbf{W}_2$ are the weighting matrices, which provide fixability to the user for emphasizing either T1 or T2 sensitivity, or emphasizing the sensitivity to the tissues with certain range of (T1, T2). The third term is to ensure the least deviation of the motion between the shared frames and the target phase p by minimizing the absolute differences between the respiratory amplitude of the shared frames (A_{t_p}) and the mean respiratory amplitude of all frames in the target phase p (A_p).

The workflow of SWIFS is illustrated in the schematic diagram in **Figure 2**. The whole process consists of 3 steps: (1) Search of shared frame, (2) calculation of DVF, and (3) motion correction (MC) of shared frames.

In step 1, the optimal inter-phase frames for the target phase were obtained by solving the minimization problem as shown in equation [12]. Genetic algorithm (GA) with integer constrain was utilized to solve the minimization problem. [27,28] To increase the convergence speed, the frame-searching was only confined to high DOM frames, namely sliding window index (SWI) #1 to 10 for T1 map optimization and SWI #45 to 55 for T2 map optimization. A more detailed discussion regarding the DOM of the frames is presented in the supporting document. It is worth mentioning that these SWI in every MRF repetitions were also included in the frame-searching. The output of the GA was a binary vector with the length equal to the total number of the confined searching frames (i.e. (10×T1 sensitive frame + 11×T2 sensitive frame) × 2 MRF repetitions = 42 frames). Inequality constrains were also specified during the optimization by GA, in which, total number of T1 and T2 sensitive frames being shared must be less than the user defined thresholds. For all the experiments, the thresholds of 3 and 4 were used for T1 and T2 frames, respectively. For every phase, GA was implemented separately, and the optimization was stopped after 50 iterations or until the stall generations of 25 were reached.

In step 2, the deformable field was calculated between each shared frame and the target phase. The goal of this step is to correct the inter-phase motion of the shared frames. A representative frame for each added frame, which was constructed by combining all frames with the respiratory amplitudes within the absolute difference of 0.02 (the surrogate signal was normalized to 0 and 1) with respect to the amplitude of the shared frame, was non-rigidly registered to the motion averaged image of the target phase to obtain the DVF. This procedure was repeated for all shared frames. The nonrigid image registration was implemented using pTV registration toolbox with default parameters. [29] Finally (step 3), the DVF was applied to the shared frame output by GA and the motion-corrected frame was allocated to the target phase bin.

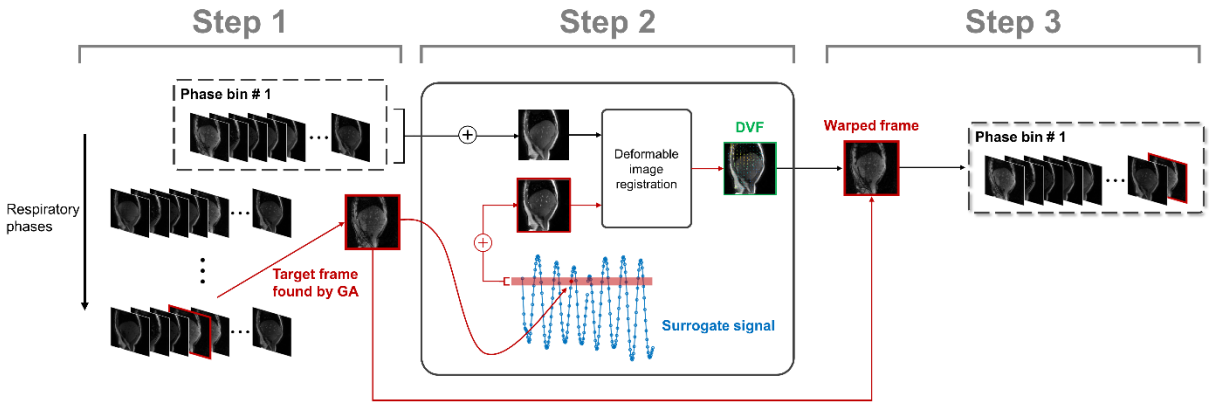

Figure 2 Workflow of the SWIFS technique. (Step 1) A representative frame was constructed by the combination of frames with similar respiratory amplitudes with respect to the target shared frame obtained by the genetic algorithm (GA), and (Step 2) nonrigidly registered to the averaged image of the target phase to obtain the deformable vector field (DVF). (Step 3) The DVF then applied to the target

shared frame for motion correction, and the motion corrected frame was allocated to the target phase. The whole process was repeated for every shared frame and every phase.

2.H Dictionary matching

The signal evolution of the reconstructed images after the modification by SWIFS was compared with the pre-computed dictionary in a voxel-by-voxel and a phase-by-phase manners. The approach used in this work was directly adopted from the original MRF paper, [10] except both the dictionary and the signal evolution were expressed in sliding window domain. [21]

2.I Simulations

Numerical simulations were performed to test the proposed SWIFS technique. MRF multi-channel k-space raw data were simulated with the same imaging sequence, k-space trajectories, and other parameters used in our in vivo scans, as mentioned in **Section 2.A**. 4D-XCAT digital phantoms [30-32] with regular and irregular breathing motions were used to generate abdominal T1 and T2 maps for the simulations. [15,16] The regular breathing pattern was a perfect sinusoidal curve with the period of 5 s. Three irregular breathing patterns were extracted and modified from the volunteer and patient scans (Figure S2). Other details regarding the implementation of the XCAT digital phantom and the assigned tissue parameters can be found in these references. [15,33,34]

2.K Quantitative analysis

The accuracy and image quality of respiratory phase-resolved T1 and T2 maps generated by numerical simulated MRF data were evaluated using intensity-based metrics, including mean absolute percentage error (MAPE), structural similarity index measure (SSIM), and peak signal-to-noise ratio (PSNR). For comparison, the SWIFS and filtered BP on SW data were used for the reconstruction of signal evolution images, followed by the identical dictionary matching strategy. The conventional approach with 8 MRF repetitions followed by simple filtered BP were also compared. These methods will be abbreviated as "SWIFS", "SW+BP(2rep)", and "BP(8rep)", respectively. The quantitative analysis was performed on the multiparametric maps reconstructed by the data with regular and irregular breathing patterns. For the simulation with irregular breathing patterns, the final quantitative results were the average measurements derived from the simulations with three breathing patterns.

The predicted T1 and T2 relaxation times of liver reconstructed by these approaches were measured and compared for in vivo data. A square ROI with a total of 100 pixels was manually drew

on a homogeneous region of liver parenchyma on the SWIFS, SW+BP(2rep), and BP(8rep) generated T1 and T2 maps for each phase. The mean and standard deviation of predicted T1 and T2 were calculated over the ROIs of all phases and all subjects.

3. RESULTS

3.A Simulations

Good image quality and inter-phase consistency can be observed in both the sagittal and coronal SWIFS generated parametric maps (**Figure 3(a), (c) and Figure 4(a), (c)**). The eight-respiratory phases T1 and T2 maps estimated by SW+ filtered BP and conventional filtered BP with 8 MRF repetitions with regular breathing pattern are shown respectively in Figure S3 and S4 for comparison. The quality of these parametric maps were suboptimal. For instance, despite the oversampling for the conventional approach, the parametric maps were corrupted by undersampling artifacts and motion artifacts, leading to high inconsistency of T1 and T2 magnitudes between phases. The parametric maps generated by three approaches with irregular breathing pattern are shown in Figure S5 - S8 as well.

The quantitative assessment of the T1 and T2 maps estimated using different approaches for regular breathing and irregular breathing phantoms are summarized in **Table 1**. For all the simulations, the SWIFS approach had superior performance in reducing overall errors and inter-phase inconsistencies of parametric maps. For instance, the mean (standard deviation) of MAPE of T1 and T2 maps generated by SWIFS in the coronal plane decreased by 36.0% (22.7%) and 72.6% (21.2%), respectively, with respect to that generated by the conventional approach. Similar results were also discernable in the predicted T1 and T2 values of different abdominal tissue types presented in **Figure 5**.

The change of T1 and T2 sensitivities in SWIFS procedure were quantified by the MD_{T1} or MD_{T2} as a function of T1 and T2 values, and the change of the metrics of two representative phases with respect to the sequential addition of sliding window frames is presented in **Figure 6 (a)** and **(b)**. In phase 4 (**Figure 6(a)**), since no T1 sensitive frame was originally allocated in this phase, the MD_{T1} of most of the abdominal tissues was very low and the dictionary matching was heavily corrupted by aliasing artifacts (Figure S3(a)). The sequential addition of T1 sensitive frames, i.e. sliding window index (SWI) # 2, 100, and 4, into this phase bin locally enhanced the MD_{T1} of $0.1\ s \leq T1 \leq 1.5\ s$ and $T2 \leq 0.08\ s$. Further addition of T2 sensitive frames, i.e. SWI # 49, 147, 50, and 148, only marginally altered the MD_{T1} of $T1 \leq 0.3\ s$. In phase 1 (**Figure 6(b)**), addition of T1 sensitive frames, i.e. SWI # 4, 5, and 103, only locally increased the MD_{T2} of high T1 and low T2 value., namely $1.0\ s \leq T1 \leq 2.0\ s$ and $T2 \leq 0.03\ s$. In contrast, the sequential addition of T2 sensitive frames, i.e. SWI # 49, 147, 50, and

148, not only increased the overall MD_{T2}, but also gradually increased the local MD_{T2} of 0.2 s ≤ T2 ≤ 0.05 s and all T1 values.

The plots of MAPE and MD_{T1} against the sequential frame addition (**Figure 6 (c)** and **(d)**) further demonstrates the relationship between the T1 and T2 sensitivities metrics and the resultant parametric maps' accuracies. Especially, the addition of first T1 and T2 sensitive frames had a potent effect on the MD_{T1} and MD_{T2}, respectively, resulting in a significant reduction in MAPE of the corresponding parametric maps.

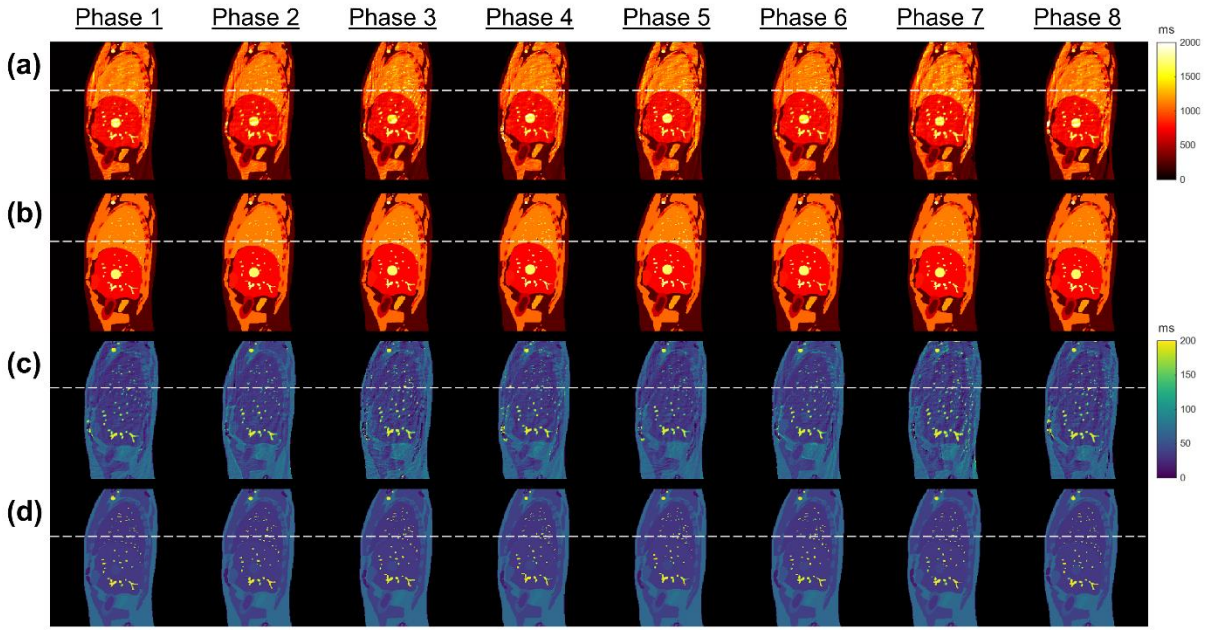

Figure 3 The T1 (a) and T2 (c) maps of 8 respiratory phases generated by 4D-MRF framework with SWIFS on XCAT phantom with regular breathing pattern in sagittal view. The corresponding ground truth T1 (b) and T2 (d) maps are presented as references. The Dashed lines indicate the diaphragm position to facilitate the visualization of respiratory motion.

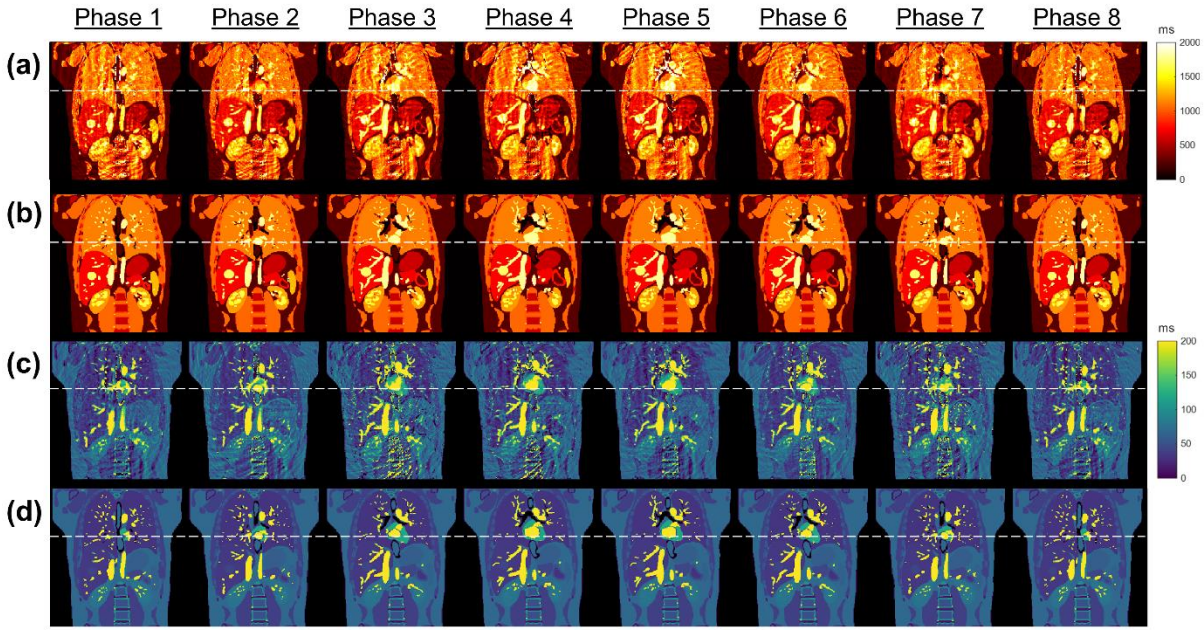

355

Figure 4 The T1 (a) and T2 (c) maps of 8 respiratory phases generated by 4D-MRF framework with SWIFS on XCAT phantom with regular breathing pattern in coronal view. The corresponding ground truth T1 (b) and T2 (d) maps are presented as references. The Dashed lines indicate the diaphragm position to facilitate the visualization of respiratory motion.

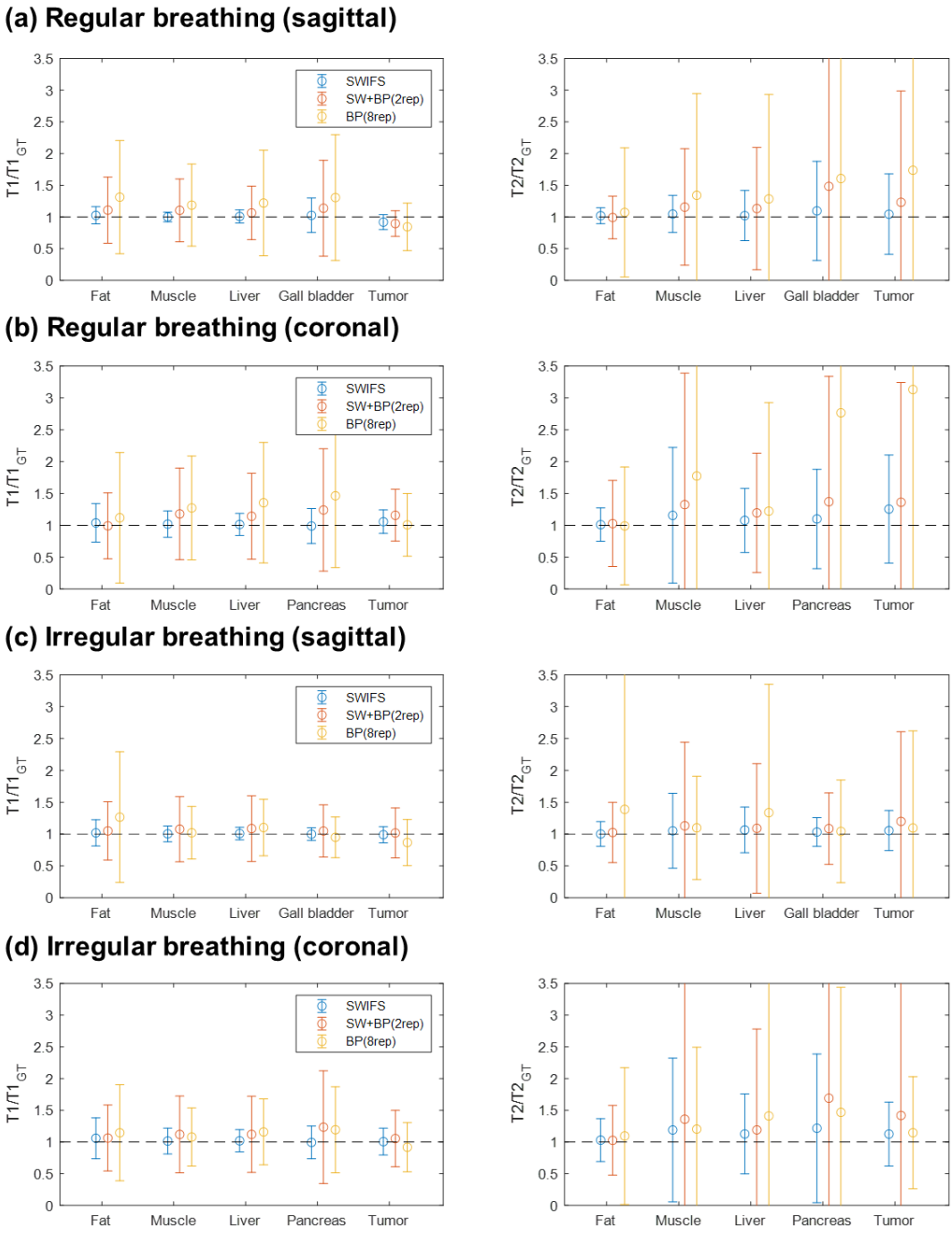

360

Figure 5 The mean value and the standard deviation (error bars) of the predicted T1 and T2 by different methods of different tissues. The predicted T1 and T2 were normalized to the corresponding ground truth values of the tissue types. The mean and the standard deviation were calculated on all the pixels of the tissue type over all 8 respiratory phases.

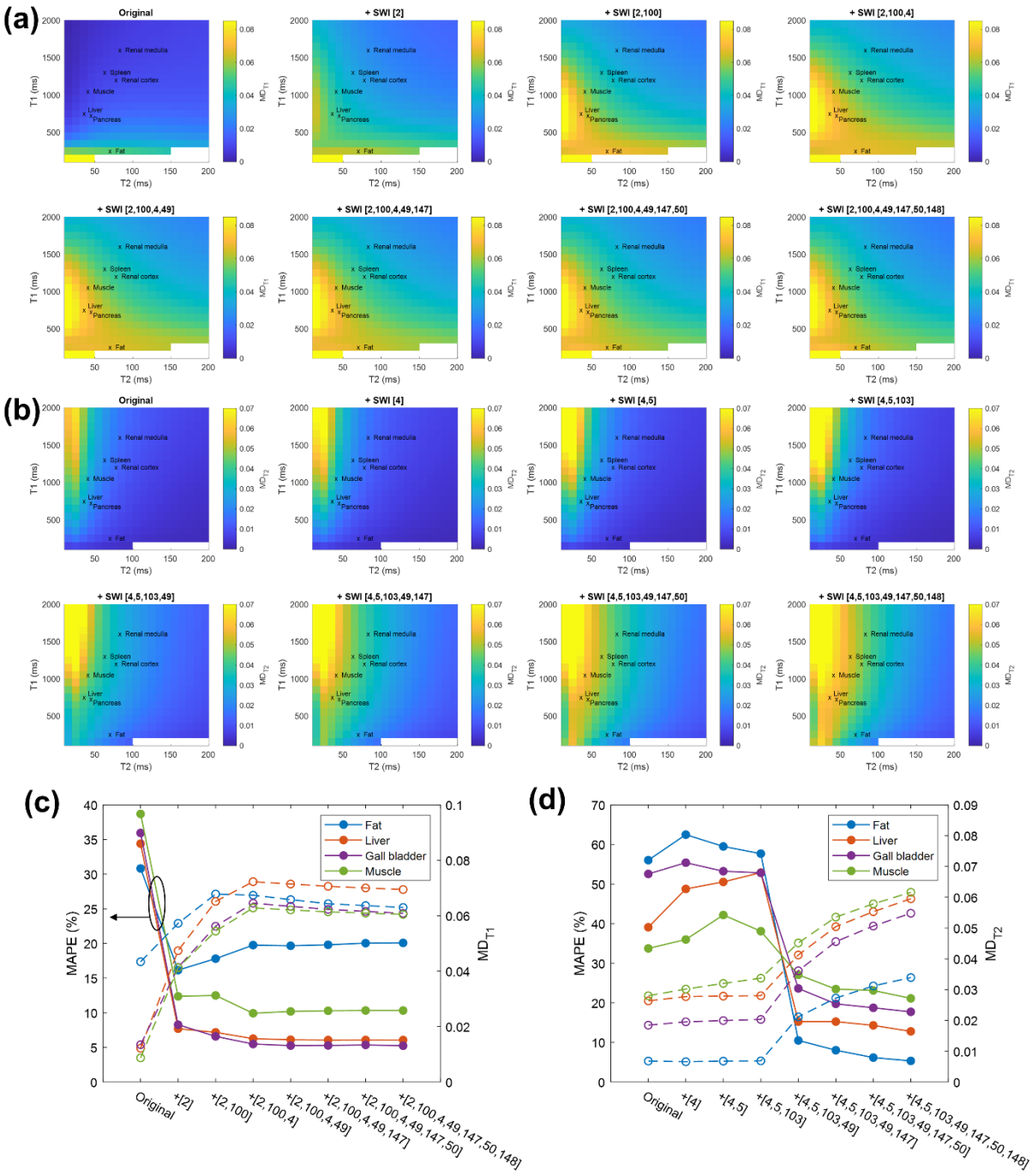

Figure 6 Changes in dictionary quantities and the resulting parametric maps' accuracies with respect to the addition of sliding window frames into the phase bin in the numerical simulations performed on XCAT phantom with regular breathing pattern in sagittal view. The MD_{T1} of phase 4 (a) and MD_{T2} of phase 1 (b) as a function of T1 and T2 relaxation times after the sequential addition of sliding window frames identified by sliding window indices (SWI). Organs with specific T1 and T2 values assigned in the numerical simulations are label in each figure. The changes in mean absolute percentage error (MAPE) of predicted T1 (c) and T2 (d) of four tissue types with respect to sequential addition of the sliding window frames corresponding to (a) and (b), respectively. The changes in MD_{T1} and MD_{T2} associated with the frame addition are also plotted in (c) and (d), respectively.

Table 1 Mean and standard deviation of the mean absolute percentage error (MAPE), structural similarity index measure (SSIM), and peak signal-to-noise ratio (PSNR) of the T1 and T2 maps generated by Sliding window inter-phase frame sharing (SWIFS) and filtered back-projection on sliding window data with 2 MRF repetitions (SW+BP(2rep)), and filtered back-projection with 8 MRF repetitions (BP(8rep)) approaches in numerical simulations.

		T1			T2		
		MAPE (%)	SSIM	PSNR	MAPE (%)	SSIM	PSNR
Regular breathing (Sagittal)	SWIFS	8.28 ± 1.63	0.79 ± 0.0134	68.0 ± 0.827	14.4 ± 2.70	0.93 ± 0.0201	34.7 ± 1.69
	SW+BP(2rep)	20.9 ± 10.8	0.66 ± 0.0782	60.3 ± 5.70	28.0 ± 7.96	0.81 ± 0.0437	27.9 ± 2.60
	BP(8rep)	36.2 ± 21.1	0.6 ± 0.0790	56.7 ± 5.69	43.6 ± 12.1	0.73 ± 0.0554	24.4 ± 1.85
Regular breathing (Coronal)	SWIFS	15.6 ± 1.53	0.58 ± 0.0189	59.9 ± 0.943	38.4 ± 7.88	0.76 ± 0.0399	22.6 ± 1.45
	SW+BP(2rep)	35.2 ± 16.9	0.44 ± 0.109	55.0 ± 3.87	61.8 ± 15.2	0.6 ± 0.0641	19.2 ± 1.23
	BP(8rep)	51.6 ± 24.2	0.38 ± 0.0991	52.9 ± 3.75	111 ± 29.1	0.47 ± 0.0686	16.6 ± 1.99
Irregular breathing (Sagittal)	SWIFS	8.62 ± 1.59	0.78 ± 0.0165	67.8 ± 0.619	16.2 ± 3.88	0.92 ± 0.0178	31.8 ± 3.12
	SW+BP(2rep)	19.4 ± 9.61	0.66 ± 0.0552	60.5 ± 4.4	27.0 ± 9.89	0.84 ± 0.0405	27.4 ± 4.46
	BP(8rep)	22.1 ± 11.0	0.64 ± 0.0492	60.1 ± 4.08	30.8 ± 14.9	0.84 ± 0.0400	25.5 ± 6.90
Irregular breathing (Coronal)	SWIFS	15.5 ± 0.999	0.58 ± 0.0173	59.8 ± 0.719	42.9 ± 6.93	0.75 ± 0.0369	20.6 ± 2.26
	SW+BP(2rep)	32.4 ± 15.1	0.45 ± 0.0764	55.5 ± 3.31	64.6 ± 22.4	0.64 ± 0.0759	18.4 ± 3.22
	BP(8rep)	33.6 ± 16.9	0.43 ± 0.0695	56.1 ± 3.15	60.2 ± 18.2	0.67 ± 0.0649	19.3 ± 3.56

3.B In vivo volunteers and patients studies

The T1 (T2) map for a liver cancer patient in the sagittal view of the representative respiratory phases generated using the SWIFS and BP approaches are presented in **Figure 7(a)** and **(b)** (**Figure 7(c)** and **(d)**), respectively. More in vivo results are presented in Figure S9, S10, and S11 for demonstration. These results revealed that the BP approach generated T1 and T2 maps, which were corrupted by undersampling artifacts due to data insufficiency in the phase bins, could be recovered by SWIFS workflow with great intra- and inter-phase precision. While for conventional approach, despite the oversampling of data by multiple MRF repetitions, inconsistent quality of parametric maps, especially in T1, were observed across different phases for two volunteers.

The overall distributions of the predicted T1 and T2 relaxation times of liver by the SWIFS, SW+BP(2rep), and BP(8rep) approaches for volunteers and by the SWIFS and SW+BP(2rep) approaches for patients across all phases are presented in Figure 8, and the associated statistical analysis

of individual subjects are summarized in Table S1. The mean T1 and T2 of liver of all subjects estimated by the SWIFS were 795 ms ± 38.9 ms and 58.3 ms ± 11.8 ms, respectively. The predicted T1 and T2 values of liver by SWIFS approach were overestimated as compared to the reported values in literature. [34] It is probably due to the field inhomogeneity effects [35] and insufficient T2 sensitivity of our MRF sequence. For SW+BP(2rep) and BP(8rep) approaches, low precision in predicted values was observed as indicated by the large standard deviation in both predicted T1 and T2 values. As deformable registration for motion correction was applied in SWIFS, the accuracy of the tumor position of a representative patient after the motion correction was evaluated and shown in Figure S12.

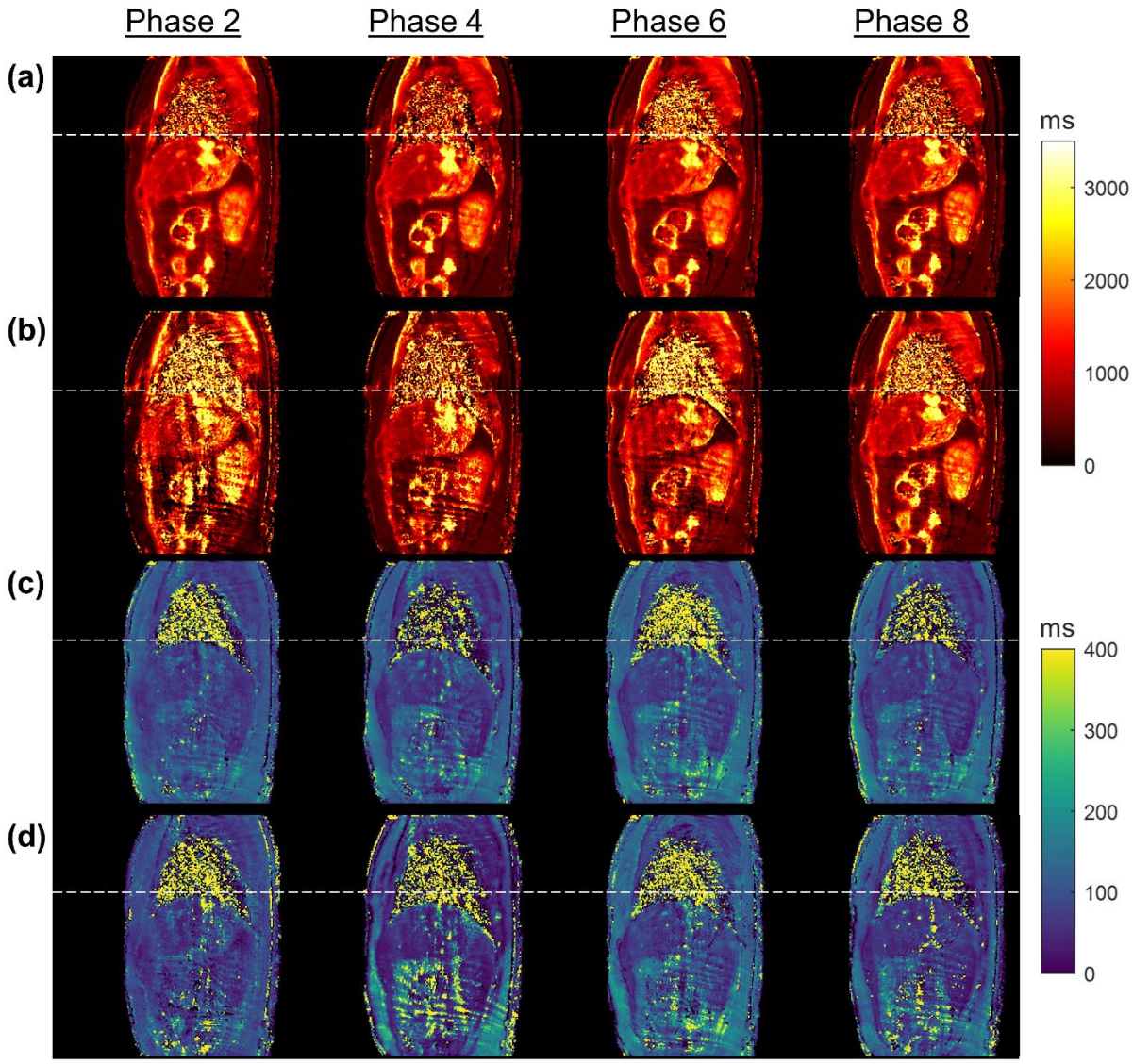

Figure 7 The T1 (a) and T2 (c) maps of 4 representative respiratory phases generated by 4D-MRF framework with SWIFS for a liver cancer patient in sagittal view. The T1 (b) and T2 (d) maps generated by SW+BP(2rep) are presented as references. The Dashed lines indicate the diaphragm position to facilitate the visualization of respiratory motion.

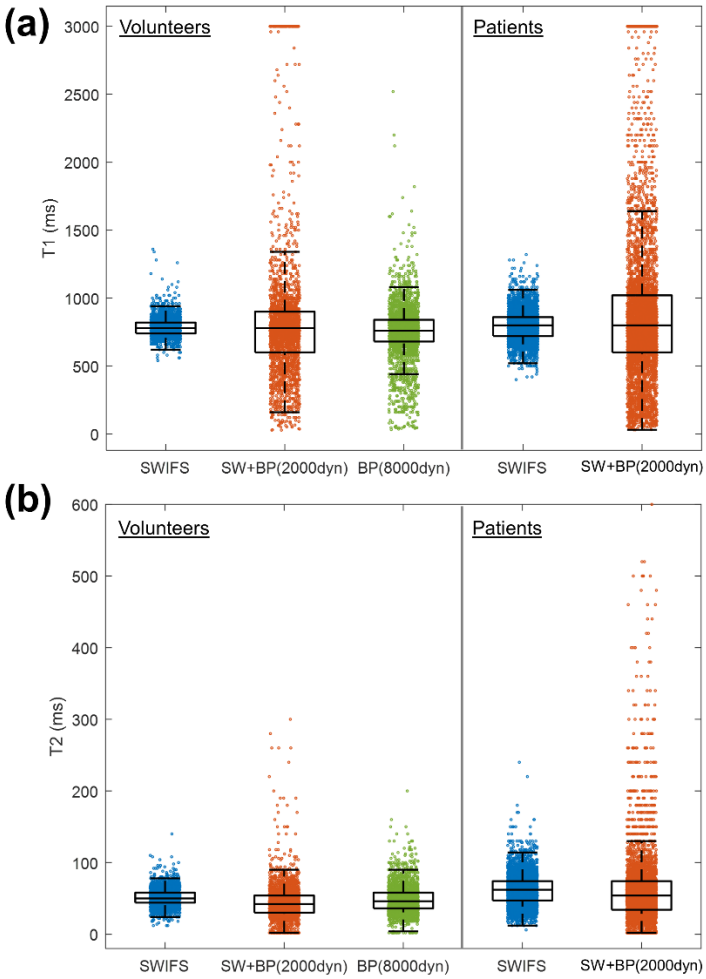

Figure 8 The predicted T1 (a) and T2 (b) relaxation times of liver parenchyma by SWIFS, SW+BP(2rep) and BP(8rep) approaches for volunteer scans and by SWIFS and SW+BP(2rep) approaches for patient scans.

5. DISCUSSION

In this work, we proposed a few metrics to quantify the T1 and T2 sensitivities of the sorted MRF signal evolution curves. We also developed a technique, SWIFS, that enhances the accuracies and precisions of respiratory phase-resolved parametric maps by the optimization of T1 and T2 sensitivities of each phase through the allocation of the motion-corrected T1 and T2 sensitive frames to compensate the data insufficiency in 4D-MRF. The SWIFS approach has been tested on XCAT simulations and in vivo experiments. The T1 and T2 maps generated using SWIFS showed reduced aliasing artifacts and increased T1 and T2 prediction precisions as compared to that generated using conventional 4D-MRF approach.

In conventional MRF, a sufficient number of time points are essential to minimize errors in dictionary matching. The errors can be attributable to two aspects, namely the aliasing artifacts and the low T1 and T2 sensitivities of the signal evolution. [9,36,37] Research has shown that MRF acquisition with a total temporal length of 500-600 yields an optimal balance between parametric maps' errors and scanning efficacy. [16,38,39] Further decreasing the temporal length can elicit the missing spatial information due to the aliasing artifacts, and greatly increases the errors in dictionary matching. [9] Besides, in abdominal free-breathing MRF, the otherwise continuous MRF signal evolution is truncated and sorted into different respiratory phases based on the surrogate signal of patient. [15,16] After the phase sorting process, on one hand, the total number of temporal frames of each phase bin can be very insufficient. On the other hand, high T1 and T2 sensitive frames may be unevenly sorted into certain bins, resulting in large variation in T1 and T2 sensitivities amid the phase bins. To solve these problems, prolonged scanning time was adopted by early works to ensure the data completeness of each bin. [15,16] However, this may inevitably sacrifice the efficacy of MRF acquisition, and it may not always perform well as shown in our reference examples in this paper. This can be illustrated by our XCAT experiment with 8 MRF repetitions and regular breathing pattern (Figure S3) that good quality of T1 and T2 maps can only be observed in certain phases as a result of uneven distribution of highly sensitive frames despite the oversampling of MRF data. Thus, T1 and T2 sensitivities in each phase bin is vital for good quality parametric maps.

One of the key features of SWIFS is that it is a technique enabled by the sliding window combination of MRF data with non-unity stride. We found that when a relatively large window size (> 10 frames) was utilized, the use of non-unity stride could greatly reduce the computational burden without compromising the accuracies of final multi-parametric maps (Figure S13 and supporting document). To balance the image sharpness and the computational burden, the window size and stride of 30 and 10 frames, respectively, were adopted in this work. As a result, the total number of frames was reduced from 2000 to 198 after the sliding window treatment of MRF data. This leaded to a great reduction in the amount of data being processed in the optimization problem and the subsequent nonrigid image registration.

The rationale of SWIFS is to tailor the optimal MRF data arrangement in each phase bin for maximizing the dictionary sensitivity. Through XCAT simulations, we found that there was a strong association between the errors of the multi-phase parametric maps and the T1 and T2 sensitivities of the corresponding phase-sorted signal evolutions (**Figure 6(c)** and **(d)**). The sorted data with low T1 and T2 sensitivities implied high similarities between the closest dictionary entries, and therefore, the dictionary matching was prone to error when the image pixel was under perturbation (e.g. aliasing artifacts). In this work, MD as a function of T1 and T2 relaxation times was utilized as a metric to quantify the T1 and T2 sensitivities of signal evolution. We further hypothesized that there is a subtle relationship amongst the DOM, T1 and T2 sensitivities, MD, and final parametric maps' quality, such

that the addition of frames with high d**D**/dT1 (d**D**/dT2), namely T1 (T2) sensitive frames, can increase the MD_{T1} (MD_{T2}) of certain range of T1 and T2, and greatly reduce the errors of the predicted tissues' T1 (T2) values. Based on this hypothesis, we formulated a minimization problem (equation [12]) to optimize the dictionary sensitivity and shared frames by merely dictionary quantities without any computationally intensive dictionary matching steps. The hypothesis has been validated by XCAT simulations, in which, the sequential addition of T1 or T2 sensitive frames locally enhanced the MD of specific range of T1 and T2, and accuracies of the resulting T1 and T2 maps largely followed the corresponding MD increments, as illustrated in **Figure 6**.

To our knowledge, three works regarding motion-corrected reconstruction of multi-phase MRF data have been recently proposed and they have shown very promising results. [23,24,40] Essentially, the full signal evolution of each phase is recovered by the nonrigid registration of the truncated signal evolutions of other phases to the target phase. However, for 2D single slice or cine acquired MRF data, the nonrigid registration in a slice-by-slice manner can potentially be a source of errors to the resulting multi-phase parametric maps due to the inter-phase through-plane motion. In contrast, the proposed SWIFS precisely targets a small number of high T1 and T2 sensitive frames, avoiding the registration of entire signal evolution. Moreover, a regularization term was added in the optimization of frame sharing (third term in equation [12]) to penalize the motion deviation from the target phase to further avoid the errors introduced by the through-plane motion. The advantages of this approach can be manifested in the coronal view (**Figure 4**), where the motion artifacts of all phases are minimal despite the significant anterior-posterior motion of organs in abdomen.

This work only aims to demonstrate feasibility of enhancing the quality and precision of the multi-phase parametric maps in 4D-MRF by manipulating the T1 and T2 sensitivity of each phase. There are numerous aspects that could improve the performance of the reconstruction technique. For instance, the contribution of undersampling pattern to the dictionary matching errors has not been investigated quantitatively in this work. [36] Minimizing the undersampling errors in a similar manner as the SWIFS approach would be possible if the relationship between the aliasing artifacts and the MRF data arrangement were identified. As to the choice of acquisition sequence, we simply adopted a popular MRF sequence with good empirical performance to demonstrate the feasibility of SWIFS strategy in this work. Nonetheless, accuracy of parametric maps is subtlety influenced by MRF sequence properties, including RF pulse train, pseudo random TR pattern, and k-space undersampling scheme. [26] The effectiveness of the proposed SWIFS approach on different MRF sequences is worth to be explored in future. For instance, the MRF sequences with multiple IR pulses and T2-preparation pulses can provide more potent T1 and T2 sensitivities to certain frames, which can increase the availability of frame selection under the SWIFS framework. Furthermore, MD as a function of T1 and T2 relaxation times for the quantification of dictionary sensitivity can potentially be utilized in sequence optimization for MRF acquisition. For instance, global MD can be used as a metric for the optimization of flip angle,

TR, and TE. [38,41,42]Regarding the numerical computation, the iterative optimization of the T1 and T2 sensitivities, nonrigid image registration, and filtered BP procedures in the proposed SWIFS framework were computationally costly. Recently, DVF estimation using deep learning technique have demonstrated to achieve high registration accuracy and very short computational time. [43] The integration of deep learning with SWIFS would be of interest in future studies. Last but not least, field inhomogeneity was ignored in this work. Although the FISP-MRF sequence is inherently insensitive to B0 inhomogeneity, [44] the large FOV of abdominal MRF imaging results in significant B1 inhomogeneity, which has been reported to exhibit an increase in T1 and T2 values. [35] For the clinical implementation of the technique, the application of field inhomogeneity correction to the reconstruction algorithm should be investigated.

6. CONCLUSION

This work has proposed a novel technique, SWIFS, that enhances the quality and precision of multi-phase parametric maps for shortened acquisition of cine or 2D free breathing abdominal MRF through the optimization of the local T1 and T2 sensitivities.

Acknowledgement

This research was partly supported by research grants of General Research Fund (GRF 15102219), the University Grants Committee, Health and Medical Research Fund (HMRF 06173276), the Food and Health Bureau, Hong Kong Special Administrative Regions, and the NSFC Young Scientist Fund (8220294) from the People's Republic of China.

Conflict of Interest

The authors declare no competing financial interests.

References

1. Li G, Citrin D, Camphausen K, et al. Advances in 4D Medical Imaging and 4D Radiation Therapy. *Technol Cancer Res Treat.* 2008;7(1):67-81.
2. Watkins WT, Li R, Lewis J, et al. Patient-specific motion artifacts in 4DCT. *Med Phys.* 2010;37(6Part1):2855-2861.
3. Tian Z, Jia X, Dong B, Lou Y, Jiang SB. Low-dose 4DCT reconstruction via temporal nonlocal means. *Med Phys.* 2011;38(3):1359-1365.

4. Wang C, Yin F-F. 4D-MRI in Radiotherapy. In: *Magnetic Resonance Imaging.* IntechOpen; 2019.
5. Stemkens B, Paulson ES, Tijssen RHN. Nuts and bolts of 4D-MRI for radiotherapy. *Phys Med Biol.* 2018;63(21):21tr01.
6. Liu Y, Zhong X, Czito BG, et al. Four-dimensional diffusion-weighted MR imaging (4D-DWI): a feasibility study. *Med Phys.* 2017;44(2):397-406.
7. Liu Y, Yin F-F, Czito BG, Bashir MR, Cai J. T2-weighted four dimensional magnetic resonance imaging with result-driven phase sorting. *Med Phys.* 2015;42(8):4460-4471.
8. Harris W, Yin F-F, Wang C, Zhang Y, Cai J, Ren L. Accelerating volumetric cine MRI (VC-MRI) using undersampling for real-time 3D target localization/tracking in radiation therapy: a feasibility study. *Phys Med Biol.* 2017;63(1):01NT01.
9. Chen Y, Lu L, Zhu T, Ma D. Technical overview of magnetic resonance fingerprinting and its applications in radiation therapy. *Med Phys.* 2022;49(4):2846-2860.
10. Ma D, Gulani V, Seiberlich N, et al. Magnetic resonance fingerprinting. *Nature.* 2013;495(7440):187-192.
11. Poorman ME, Martin MN, Ma D, et al. Magnetic resonance fingerprinting Part 1: Potential uses, current challenges, and recommendations. *J Magn Reson Imaging.* 2020;51(3):675-692.
12. Liu C, Li M, Xiao H, et al. Advances in MRI-guided precision radiotherapy. *Precision Radiation Oncology.* 2022;6(1):75-84.
13. Ding H, Velasco C, Ye H, et al. Current Applications and Future Development of Magnetic Resonance Fingerprinting in Diagnosis, Characterization, and Response Monitoring in Cancer. *Cancers (Basel).* 2021;13(19):4742.
14. Liu C, Li T, Cao P, et al. Respiratory-Correlated 4-Dimensional Magnetic Resonance Fingerprinting for Liver Cancer Radiation Therapy Motion Management. *Int J Radiat Oncol Biol Phys.* 2023.
15. Li T, Cui D, Hui ES, Cai J. Time-resolved magnetic resonance fingerprinting for radiotherapy motion management. *Med Phys.* 2020;47(12):6286-6293.
16. Li T, Cui D, Ren G, Hui ES, Cai J. Investigation of the effect of acquisition schemes on time-resolved magnetic resonance fingerprinting. *Phys Med Biol.* 2021;66(9):095013.
17. Assländer J, Cloos MA, Knoll F, Sodickson DK, Hennig J, Lattanzi R. Low rank alternating direction method of multipliers reconstruction for MR fingerprinting. *Magn Reson Med.* 2018;79(1):83-96.
18. Davies M, Puy G, Vandergheynst P, Wiaux Y. A Compressed Sensing Framework for Magnetic Resonance Fingerprinting. *SIAM Journal on Imaging Sciences.* 2014;7(4):2623-2656.
19. Wang Z, Li H, Zhang Q, Yuan J, Wang X. Magnetic resonance fingerprinting with compressed sensing and distance metric learning. *Neurocomputing.* 2016;174:560-570.
20. Zhao B, Setsompop K, Ye H, Cauley SF, Wald LL. Maximum Likelihood Reconstruction for Magnetic Resonance Fingerprinting. *IEEE Trans Med Imaging.* 2016;35(8):1812-1823.
21. Cao X, Liao C, Wang Z, et al. Robust sliding-window reconstruction for Accelerating the acquisition of MR fingerprinting. *Magn Reson Med.* 2017;78(4):1579-1588.
22. Bipin Mehta B, Coppo S, Frances Mcgivney D, et al. Magnetic resonance fingerprinting: a technical review. *Magn Reson Med.* 2019;81(1):25-46.
23. Hamilton JI, Jiang Y, Eck B, Griswold M, Seiberlich N. Cardiac cine magnetic resonance fingerprinting for combined ejection fraction, T1 and T2 quantification. *NMR Biomed.* 2020;33(8).
24. Cruz G, Qi H, Jaubert O, et al. Generalized low-rank nonrigid motion-corrected reconstruction for MR fingerprinting. *Magn Reson Med.* 2022;87(2):746-763.
25. Weigel M. Extended phase graphs: Dephasing, RF pulses, and echoes - pure and simple. *J Magn Reson Imaging.* 2015;41(2):266-295.
26. Stolk CC, Sbrizzi A. Understanding the Combined Effect of k-Space Undersampling and Transient States Excitation in MR Fingerprinting Reconstructions. *IEEE Trans Med Imaging.* 2019;38(10):2445-2455.
27. Deb K. An introduction to genetic algorithms. *Sadhana.* 1999;24(4-5):293-315.

28. Conn AR, Gould N, Toint PL. A globally convergent Lagrangian barrier algorithm for optimization with general inequality constraints and simple bounds. *Mathematics of Computation.* 1997;66(217):261-289.
29. Vishnevskiy V, Gass T, Szekely G, Tanner C, Goksel O. Isotropic Total Variation Regularization of Displacements in Parametric Image Registration. *IEEE Trans Med Imaging.* 2017;36(2):385-395.
30. Panta RK, Segars P, Yin F-F, Cai J. Establishing a framework to implement 4D XCAT phantom for 4D radiotherapy research. *J Cancer Res Ther.* 2012;8(4):565.
31. Segars WP, Sturgeon G, Mendonca S, Grimes J, Tsui BMW. 4D XCAT phantom for multimodality imaging research. *Med Phys.* 2010;37(9):4902-4915.
32. Segars WP, Tsui BMW, Cai J, Yin F-F, Fung GSK, Samei E. Application of the 4-D XCAT Phantoms in Biomedical Imaging and Beyond. *IEEE Trans Med Imaging.* 2018;37(3):680-692.
33. Bojorquez JZ, Bricq S, Acquitter C, Brunotte F, Walker PM, Lalande A. What are normal relaxation times of tissues at 3 T? *Magn Reson Imaging.* 2017;35:69-80.
34. Stanisz GJ, Odrobina EE, Pun J, et al. T1, T2 relaxation and magnetization transfer in tissue at 3T. *Magn Reson Med.* 2005;54(3):507-512.
35. Chen Y, Jiang Y, Pahwa S, et al. MR Fingerprinting for Rapid Quantitative Abdominal Imaging. *Radiology.* 2016;279(1):278-286.
36. Körzdörfer G, Pfeuffer J, Kluge T, et al. Effect of spiral undersampling patterns on FISP MRF parameter maps. *Magn Reson Imaging.* 2019;62:174-180.
37. Kara D, Fan M, Hamilton J, Griswold M, Seiberlich N, Brown R. Parameter map error due to normal noise and aliasing artifacts in MR fingerprinting. *Magn Reson Med.* 2019;81(5):3108-3123.
38. Sommer K, Amthor T, Doneva M, Koken P, Meineke J, Börnert P. Towards predicting the encoding capability of MR fingerprinting sequences. *Magn Reson Imaging.* 2017;41:7-14.
39. Sommer K, Amthor T, Koken P, Meineke J, Doneva M. Determination of the optimum pattern length of MRF sequences. Paper presented at: Proceedings of the 25th Annual Meeting of ISMRM2017.
40. Cao P, Wang Z, Liu C, Li T, Hui E, Cai J. Motion-resolved and free-breathing liver MRF. *Magn Reson Imaging.* 2022.
41. Cohen O, Rosen MS. Algorithm comparison for schedule optimization in MR fingerprinting. *Magn Reson Imaging.* 2017;41:15-21.
42. Liu Y, Buck JR, Ikonomidou VN. Generalized min-max bound-based MRI pulse sequence design framework for wide-range T1 relaxometry: A case study on the tissue specific imaging sequence. *PLoS One.* 2017;12(2):e0172573.
43. Xiao H, Ni R, Zhi S, et al. A dual-supervised deformation estimation model (DDEM) for constructing ultra-quality 4D-MRI based on a commercial low-quality 4D-MRI for liver cancer radiation therapy. *Med Phys.* 2022;49(5):3159-3170.
44. Jiang Y, Ma D, Seiberlich N, Gulani V, Griswold MA. MR fingerprinting using fast imaging with steady state precession (FISP) with spiral readout. *Magn Reson Med.* 2015;74(6):1621-1631.

Supporting information

Table S1 Mean and standard deviation of the liver's T1 and T2 values extracted in the T1 and T2 maps generated by the SWIFS, SW+BP(2rep), and BP(8rep) approaches for each volunteer and patient in the in vivo study.

Figure S1 The readout trajectory, variation of TR and variation of flip angle against time utilized in the MRF acquisition in this work.

Figure S2 Regular breathing pattern and irregular breathing patterns used in the numerical simulations. The color of the curves represents different MRF repetitions.

Figure S3 The T1 (a, c) and T2 (b, d) maps of 8 respiratory phases generated by sliding window followed by filtered back-projection with 2 MRF repetitions (SW+BP(2rep)) (a, c) and simple filtered back-projection with 8 MRF repetitions (BP(8rep)) (b, d) on XCAT phantom with regular breathing pattern in sagittal view. The Dashed lines indicate the diaphragm position to facilitate the visualization of respiratory motion.

Figure S4 The T1 (a, c) and T2 (b, d) maps of 8 respiratory phases generated by sliding window followed by filtered back-projection with 2 MRF repetitions (SW+BP(2rep)) (a, c) and simple filtered back-projection with 8 MRF repetitions (BP(8rep)) (b, d) on XCAT phantom with regular breathing pattern in coronal view. The Dashed lines indicate the diaphragm position to facilitate the visualization of respiratory motion.

Figure S5 The T1 (a) and T2 (c) maps of 8 respiratory phases generated by 4D-MRF framework with SWIFS on XCAT phantom with a representative irregular breathing pattern in sagittal view. The corresponding ground truth T1 (b) and T2 (d) maps are presented as references. The Dashed lines indicate the diaphragm position to facilitate the visualization of respiratory motion.

Figure S6 The T1 (a) and T2 (c) maps of 8 respiratory phases generated by 4D-MRF framework with SWIFS on XCAT phantom with a representative irregular breathing pattern in coronal view. The corresponding ground truth T1 (b) and T2 (d) maps are presented as references. The Dashed lines indicate the diaphragm position to facilitate the visualization of respiratory motion.

Figure S7 The T1 (a, c) and T2 (b, d) maps of 8 respiratory phases generated by sliding window followed by filtered back-projection with 2 MRF repetitions (SW+BP(2rep)) (a, c) and simple filtered back-projection with 8 MRF repetitions (BP(8rep)) (b, d) on XCAT phantom with a representative irregular breathing pattern in sagittal view. The Dashed lines indicate the diaphragm position to facilitate the visualization of respiratory motion.

Figure S8 The T1 (a, c) and T2 (b, d) maps of 8 respiratory phases generated by sliding window followed by filtered back-projection with 2 MRF repetitions (SW+BP(2rep)) (a, c) and simple filtered back-projection with 8 MRF repetitions (BP(8rep)) (b, d) on XCAT phantom with a representative irregular breathing pattern in coronal view. The Dashed lines indicate the diaphragm position to facilitate the visualization of respiratory motion.

Figure S9 The T1 (a) and T2 (d) maps of 4 representative respiratory phases generated by 4D-MRF framework with SWIFS for a health volunteer in sagittal view. The T1 (b) and T2 (e) maps generated by SW+BP(2rep), and the T1 (c) and T2 (f) maps generated by BP(8rep) are presented as references. The Dashed lines indicate the diaphragm position to facilitate the visualization of respiratory motion.

Figure S10 The T1 (a) and T2 (d) maps of 4 representative respiratory phases generated by 4D-MRF framework with SWIFS for a health volunteer in sagittal view. The T1 (b) and T2 (e) maps generated by SW+BP(2rep), and the T1 (c) and T2 (f) maps generated by BP(8rep) are presented as references. The Dashed lines indicate the diaphragm position to facilitate the visualization of respiratory motion.

Figure S11 The T1 (a) and T2 (c) maps of 4 representative respiratory phases generated by 4D-MRF framework with SWIFS for a liver cancer patient in sagittal view. The T1 (b) and T2 (d) maps generated by SW+BP(2rep) are presented as references. The Dashed lines indicate the diaphragm position to facilitate the visualization of respiratory motion.

Figure S12 A demonstration of the accuracy of deformable registration by the tumor motion of a representative patient. (a) The tumor was segmented on the fixed image, moving images, and warped images obtained by the frame searching process in a representative phase. The conformity indices of the frames (c) were calculated as illustrated in (b).

Figure S13 Gradient entropy (a), Normalized root-mean-square error (NRMSE) (b), peak signal-to-noise ratio (PSNR) (c), structural similarity (SSIM) index, and Minkowski distance (MD) of liver of resultant T1 and T2 maps generated by sliding window reconstruction with different window size and stride.

Figure S14 $d\mathbf{D}/dT1$ with respect to the sliding window indices and T1 values for T2 = 30 ms, 50 ms and 80 ms (a), and $d\mathbf{D}/dT1$ with respect to the sliding window indices and T2 values for T1 = 300 ms, 500 ms and 800 ms (b). "×" in the plots indicates the position of the maxima.

Figure S15 $d\mathbf{D}/dT2$ with respect to the sliding window indices and T1 values for T1 = 300 ms, 500 ms and 800 ms (a), and $d\mathbf{D}/dT1$ with respect to the sliding window indices and T2 values for T2 = 30 ms, 50 ms and 80 ms (b). "×" and "○" in the plots indicate the position of the maxima and minima, respectively.

Figure S16 The $d\mathbf{D}/dT1$ and $d\mathbf{D}/dT2$ with respect to the sliding window index for several common tissues in abdomen.

Figure S17 The $\Delta\mathbf{MD}_{T1}$ (a) and $\Delta\mathbf{MD}_{T2}$ (b) of representative phases as a function of T1 and T2 relaxation times after the addition of sliding window frames identified by sliding window indices (SWI). Organs with specific T1 and T2 values assigned in the numerical simulations are labeled in each figure.

Figure S18 The $\Delta\mathbf{MD}_{T1}$ (a) and $\Delta\mathbf{MD}_{T2}$ (b) of representative phases as a function of T1 and T2 relaxation times after the addition of sliding window frames identified by sliding window indices (SWI). Organs with specific T1 and T2 values assigned in the numerical simulations are labeled in each figure.